PNAS

Supporting information for

Triggered Lattice-Oxygen Oxidation with Active-Site Generation and Self-Termination of Surface Reconstruction During Water Oxidation

Yicheng Wei,[1,#] Yang Hu,[1,#] Pengfei Da,[1] Zheng Weng,[1] Pinxian Xi*[1,2] and Chun-Hua Yan[1,3]

[1] State Key Laboratory of Applied Organic Chemistry, Frontiers Science Center for Rare Isotopes, College of Chemistry and Chemical Engineering, Lanzhou University, Lanzhou, 730000 China

[2] State Key Laboratory of Baiyunobo Rare Earth Resource Researches and Comprehensive Utilization, Baotou Research Institute of Rare Earths Baotou 014030 China

[3] Beijing National Laboratory for Molecular Sciences, State Key Laboratory of Rare Earth Materials Chemistry and Applications, PKU-HKU Joint Laboratory in Rare Earth Materials and Bioinorganic Chemistry, College of Chemistry and Molecular Engineering, Peking University, Beijing, 100871 China

*Corresponding authors. E-mails: xipx@lzu.edu.cn

[#]Equally contributed to this work.

Conflict of interest statement. There are no conflicts to declare.

This Word file includes:

Methods

Figures S1 to S34

Tables S1 to S8

Methods

Physicochemical Characterizations. XRD measurements were carried out on Rigaku MiniFlex 600 diffractometer with Cu Kα radiation (λ = 0.1542 nm) from 10° to 80° under a constant voltage of 40 kV. The Brunauer-Emmett-Teller (BET) specific surface area was determined using N_2 sorption isotherm measurements at −196 °C on Micrometrics TriStar 3020 equipment.

The morphology and EDX mapping of samples were analyzed by Thermo Fisher Apreo S filed-emission scanning electron microscopy (FESEM) at an acceleration voltage of 30 kV. Elemental mappings were performed on the Tecnai G2 F30 Field Emission Transmission Electron Microscope. Atomic-scale STEM images were recorded on a probe aberration-corrected STEM (Cubed Titan G2 60-300, FEI, USA) operated at 300 kV. Inductively coupled plasma optical emission spectrometry (ICP-OES) analyses were performed on a Plasma Quant PQ9000 ICP spectrometer. Inductively coupled plasma mass spectrometry (ICP-MS) analyses were performed on an iCAPQc spectrometer.

X-ray photoelectron spectroscopy (XPS) analysis was made with a Kratos Axis Supra device and the data obtained was corrected with C 1s line at 284.8 eV. Synchrotron radiation X-ray absorption fine structure (XAFS) spectroscopy at the Co K-edge and O K-edge were acquired in transmission mode using a Si (111) double-crystal monochromator at the 1W1B station of the Beijing Synchrotron Radiation Facility (BSRF).

Single-pulse ^{27}Al MAS NMR spectra were recorded on a Bruker 600 MHz spectrometer at 130.33 MHz (11.7 T magnet) using a standard Bruker 2.5 mm MAS probe with a 30 kHz typical spinning frequency. The spectral width was set to 0.5 MHz and the recycle time to D_0 = 5 s, long enough to avoid T_1 saturation effects. As ^{27}Al is a strong quadrupolar nucleus with I = 5/2, a short pulse length of 1.1 μs corresponding to a π/12 pulse determined using an aqueous 1 M $Al(NO_3)_3$ solution was employed. In these conditions, all of the −1/2 → +1/2 central transitions are equally excited regardless of the magnitude of the nuclear quadrupole coupling constants and one can extract quantitative data. The external reference was a 1 M $Al(NO_3)_3$ aqueous solution. For the samples containing only 4% of Al, overnight experiments (10240 scans) were carried out to ensure a good signal/noise ratio. No baseline subtraction was done in the Fig.s presented here.(1)

Electrochemical Measurements. All of the electrochemical measurements were conducted using a CHI760E potentiostat in a typical three-electrode setup with O_2-saturated 1 M KOH solution. A Pt-foil as the counter electrode and Hg/HgO with 1 M KOH filling solution as the reference electrode. The as-measured potentials (versus Hg/HgO) were calibrated with respect to the RHE. A glassy carbon electrode with a diameter of 3 mm covered by a thin catalyst film was used as the working electrode. Typically, 4 mg catalyst and 2 mg acetylene black were suspended in 1.96 mL isopropanol-water solution with a volume ratio of 3:1 and 40 μL Na^+ exchanged Nafion solution to form a homogeneous ink assisted by ultrasound for 3 h. Then, 7.2 μL of the ink was spread onto the surface of the glassy carbon electrode (mass loading: 0.20 mg cm^{-2}). For cyclic voltammetry (CV) measurements, the scan rate was set to 10 mV s^{-1}. Every 50 cycles a cyclic voltammetry between 1.0 and 1.7 V RHE at 10 mV s^{-1} has been recorded. The potentials were corrected to compensate for the effect of solution resistance and calculated using the following equation: $E_{iR\ corrected} = E - iR$, where R is the uncompensated ohmic solution resistance measured via iR compensation module in CHI760E with comp level of 95%. The Tafel slope was calculated by the equation below: $\eta = a + b \times logj$, where η stands for the overpotential, b stands for the Tafel slope, j stands for the current density. And the electrochemical impedance spectroscopy (EIS) tests were performed at open-circuit

potentials in the frequency range of 0.01 – 100 kHz in 1 M KOH. The electrochemical active surface area (ECSA) of catalyst was calculated by the equation: ECSA = C_{dl}/C_s. Where C_s is the specific capacitance of planar surface with an atomically smooth under identical electrolyte conditions. We use general value of 40 μF cm^{-2}. (2) All currents were normalized using BET specific surface area.

Magnetic calculation formula:

The susceptibility follows Curie Weiss's law:

$$1/\chi = (T - \theta)/C$$

Where C is the Curie constant while θ is the Curie–Weiss constant. Based on this, the slopes of the linear plots of χ^{-1}–T, 1/C, could be obtained. Thus, the effective magnetic moments (μ_{eff}), which correlates the number of electrons in Co e_g state, could be estimated by:

$$\mu_{eff} = 2.84 \times (C/2)^{1/2}$$

Thus, the effective magnetic moment (μ_{eff}), which correlates the number of electrons in the Co e_g state, could be estimated by $\mu_{eff} = 8C\ \mu_B$. Using the obtained values of μ_B, the volume fractions of Co ions in HS and LS states can be calculated from the following relationship:

$$\mu_{eff} = g\ \mu_B \sqrt{S_{HS}(S_{HS}+1)V_{HS} + S_{LS}(S_{LS}+1)V_{LS}}$$

where S_{HS} (= 2) and S_{LS} (= 0) are the S values, and V_{HS} and V_{LS} (= 1 − V_{HS}) are the volume fractions for Co ions in HS and LS states, respectively.

Hall measurements calculation formula:

To explore the physical nature of the transition in the electron transport property, the Hall measurements were carried out to determine the carrier concentration (n_e) and the Hall mobility (μ_H) of the series of LSCAOs at room temperature. We observed a sharply increase of carrier concentration from ≈ E+14 to ≈ 3.5E+15 cm^{-3} with the LSCAOs volume fraction along with a subsequent decrease in the mobility. The relationship between the resistivity, the carrier concentration, and the Hall mobility can be deduced from

$$\rho = 1/q\ n_e\ \mu_H$$

where q is the electric charge. Thus, the resistivity is determined by the product of n_e and μ_H values.

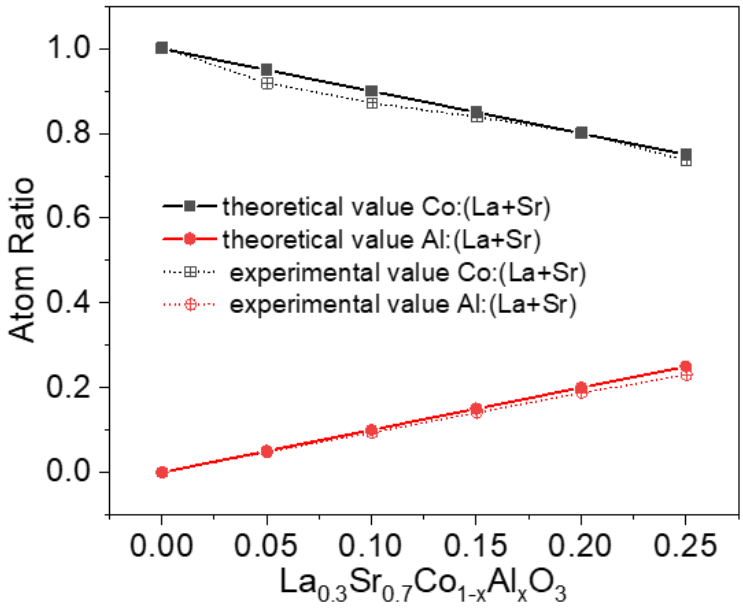

Fig. S1. Metallic element composition of LSCAOs. The relative metal ratio of as synthesis LSCAOs sample from ICP-OES tests, and details about elemental atomic percentage is shown in Supplementary Table S1.

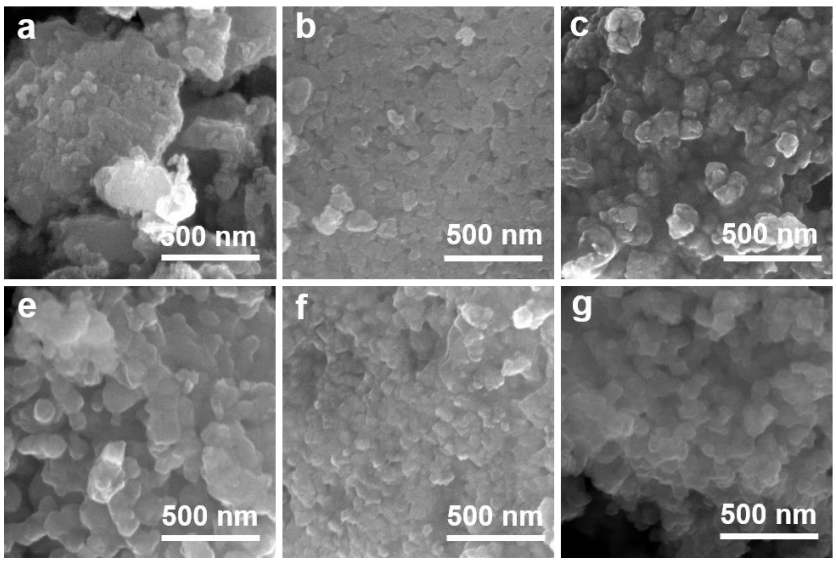

Fig. S2. SEM images of LSCAOs. (a) x=0; (b) x=0.05; (c) x=0.10; (d) x=0.15; (e) x=0.20; (f) x=0.25.

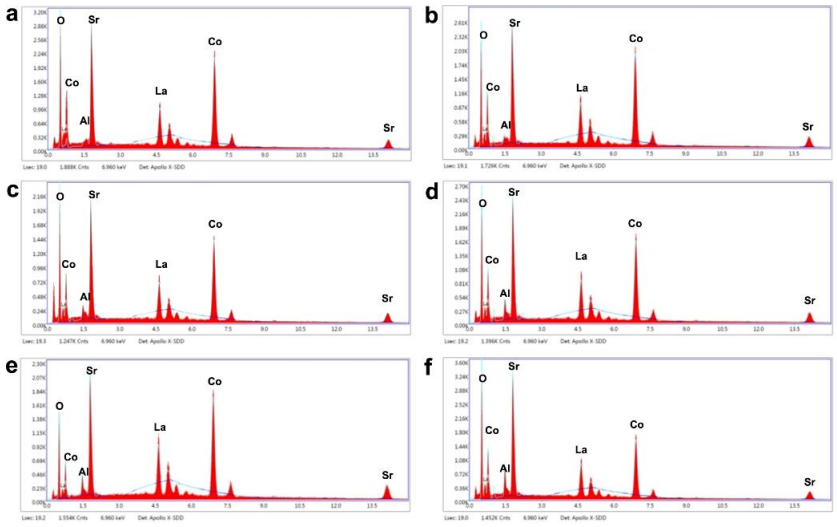

Fig. S3. The corresponding EDS elemental images of LSCAOs. (a) x=0; (b) x=0.05; (c) x=0.10; (d) x=0.15; (e) x=0.20; (f) x=0.25.

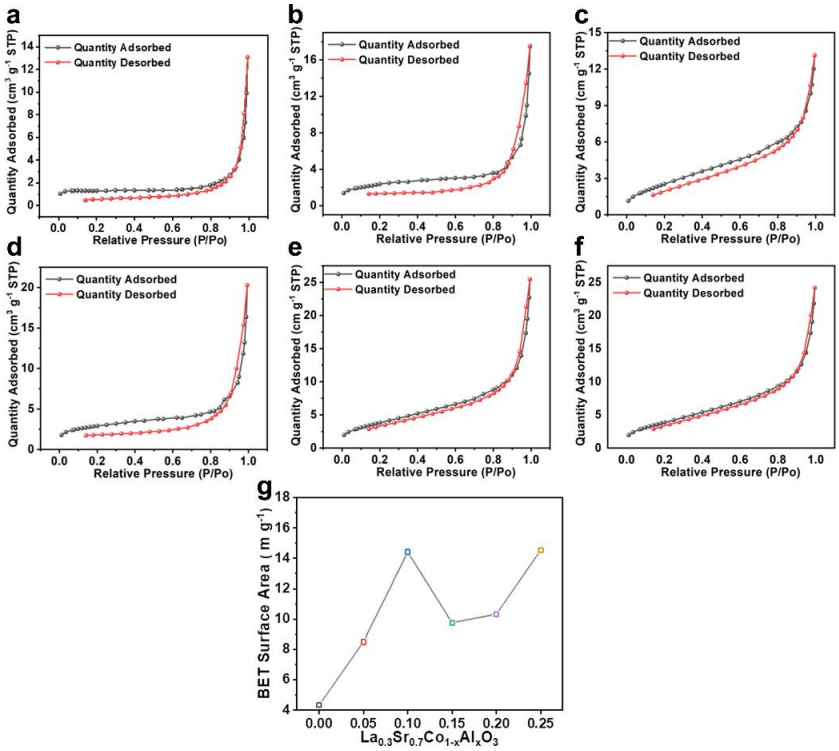

Fig. S4. The BET measurements of LSCAOs. (a) x=0; (b) x=0.05; (c) x=0.10; (d) x=0.15; (e) x=0.20; (f) x=0.25. (g) Trend in specific surface area with Al substitution.

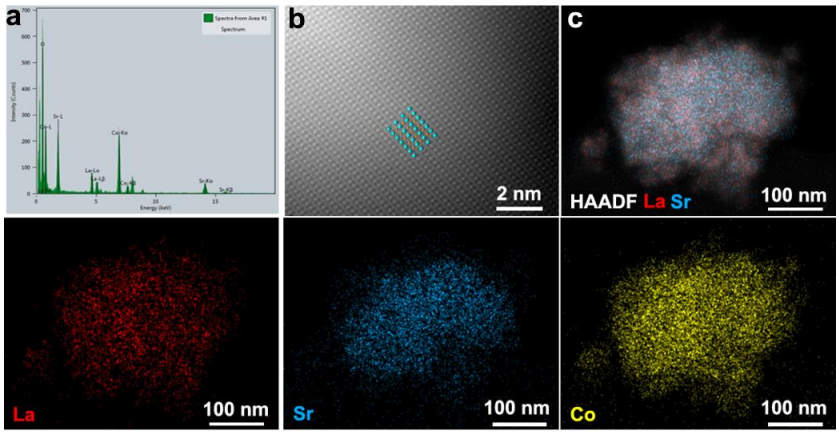

Fig. S5. The atomic arrangement and element distribution of LSCO. (a) The EDS elemental. (b) The HAADF-STEM image. (c) The EDS elemental mappings.

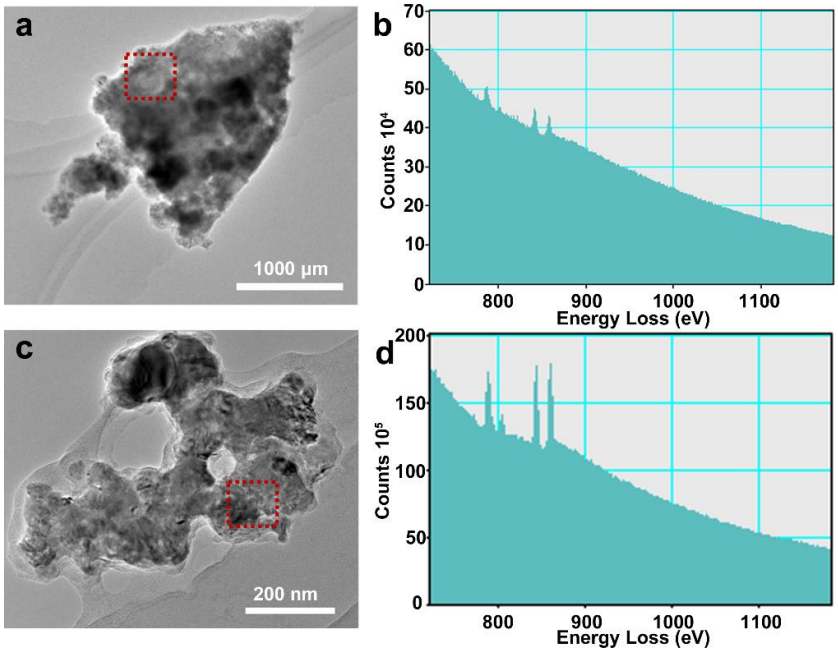

Fig. S6. The HR-TEM image and the experimental EELS spectra. (a) The HR-TEM image and (b) the experimental EELS spectra of LSCO. (c) The HR-TEM image and (d) the experimental EELS spectra of LSCAO-0.20.

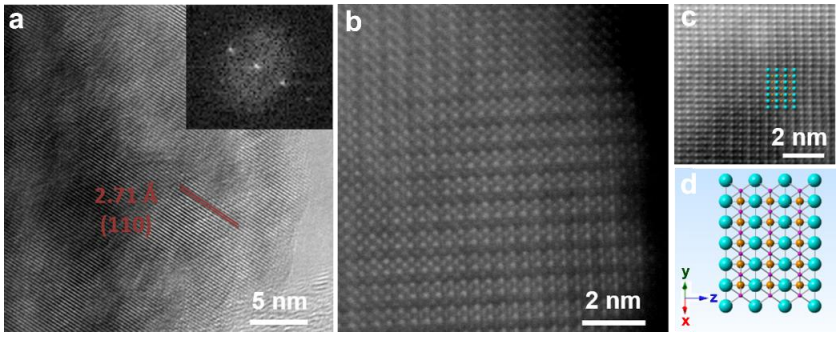

Fig. S7. The atomic arrangement of LSCO-0.20. (a) The HR-TEM image. (b) The HAADF-STEM image. (c) The enlarged HAADF-STEM image of b, (d) Corresponding standard [111] crystal structure.

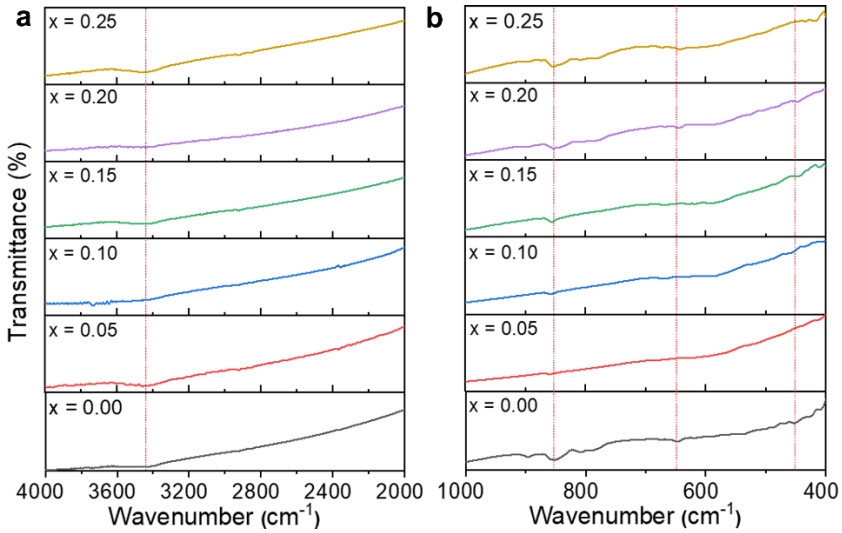

Fig. S8. FT-IR patterns of LSCAOs. A characteristic absorption band at 429 cm^{-1} is assigned to O−Co−O deformation modes in the CoO_6 octahedron and absorption band at 610 is attributed to Co−O stretching vibration.

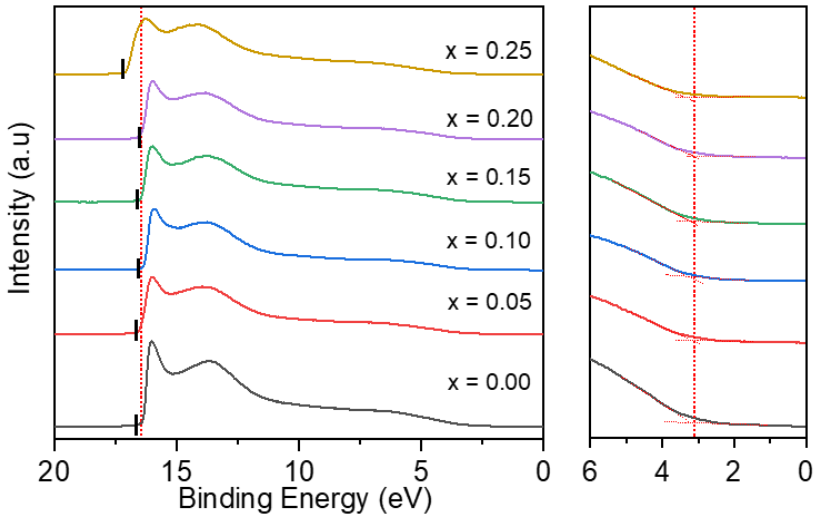

Fig. S9. UPS spectras of as-prepared series LSCAOs.

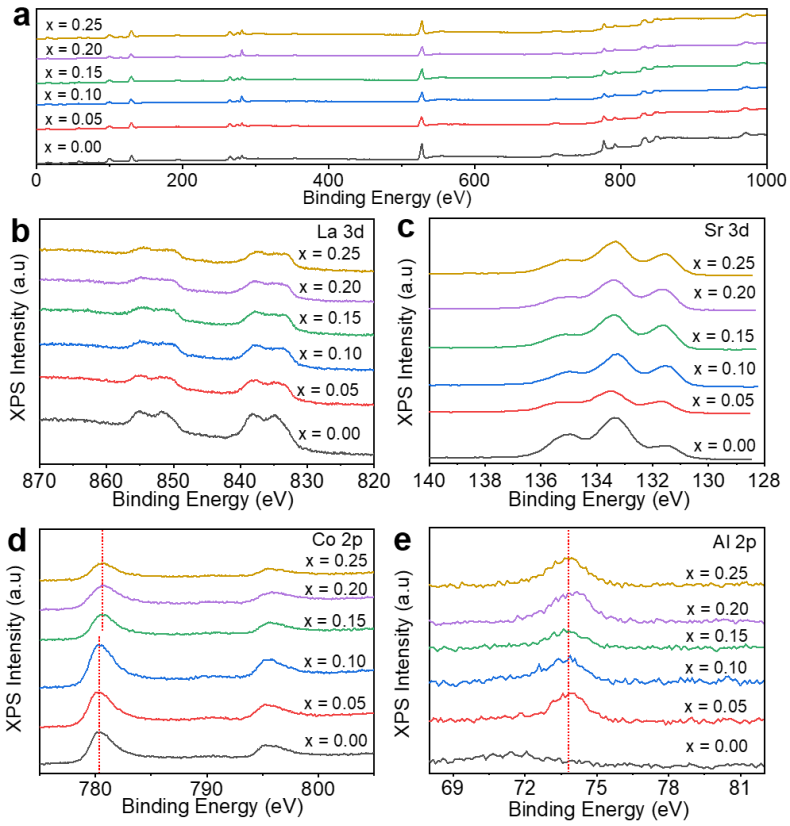

Fig. S10. The XPS surveys of as-prepared series of LSCAOs. (a) XPS survey spectrum; (b) La 3*d*; (c) Sr 3*d*; (d) Co 2*p*; (e) Al 2*p*. The La 3*d*, Sr 3*d* and Al 2*p* XPS of these samples remain unchanged, but its Co 2*p* peak of these samples slightly shifts to higher binding energy with the increase of Al concentration and its Co^{4+} and Co^{2+} contents have relative increase compared with pure LSCO. This result suggests that electron transfer leads to redistribution in the valence state of cobalt ions.

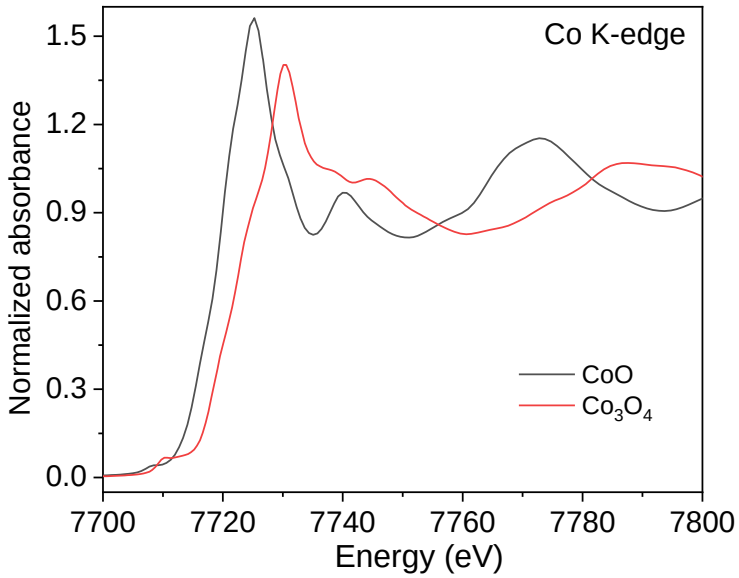

Fig. S11. Co K-edge XANES adsorption edges of Co K-edge EXAFS for CoO and Co_3O_4. The oxygen defects contents (δ) was calculated based on the principle of electric neutrality and stoichiometry.

To be specific, in $La_{0.3}Sr_{0.7}Co_{1-x}Al_xO_{3-\delta}$, the valence state of La, Sr and Al is +3, +2 and +3, respectively. The valence state of Co (denoted as a) was characterized by XAFS. So, the total positive charge in $La_{0.3}Sr_{0.7}Co_{1-x}Al_xO_{3-\delta}$ is 0.3*3 + 0.7*2 + 3*x + a*(1−x), and the total negative charge is 2*(3−δ). The total positive charge is equal to the total negative charge. Therefore, the oxygen defects contents (δ) can be calculated. Furthermore, the valence state of Co is calculated by the absorption edge position of Co K-edge XANES spectrum. The edge position and valence state of Co K-edge XANES of standard samples CoO and Co_3O_4 are taken as independent and dependent variables to obtain a linear equation. Then the edge position of Co K-edge XANES of the actual sample is substituted into the linear equation to calculate its corresponding valence state.

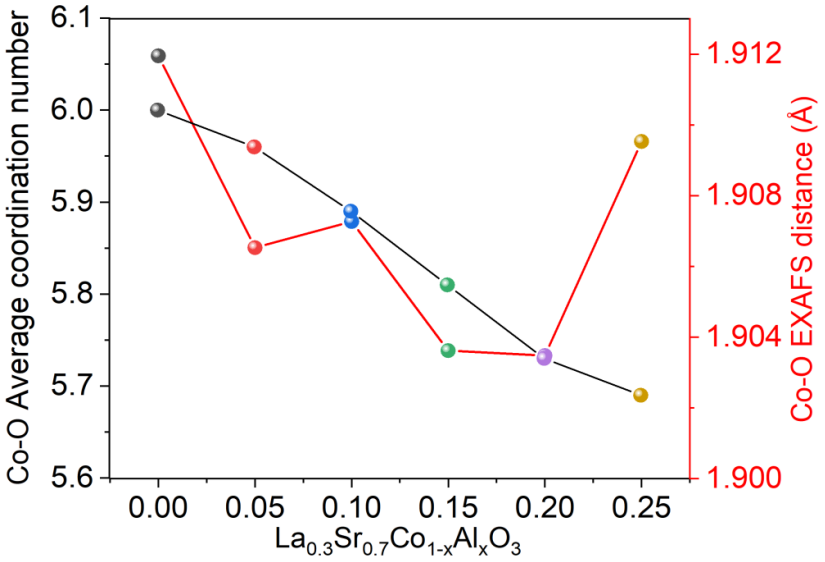

Fig. S12. Average coordination number and Co−O EXAFS distance of series of LSCAOs. The K-edge position is determined by an integral method as described in the Methods, and the details about edge positions and nominal valence state of Co is shown in Supplementary Table S3.

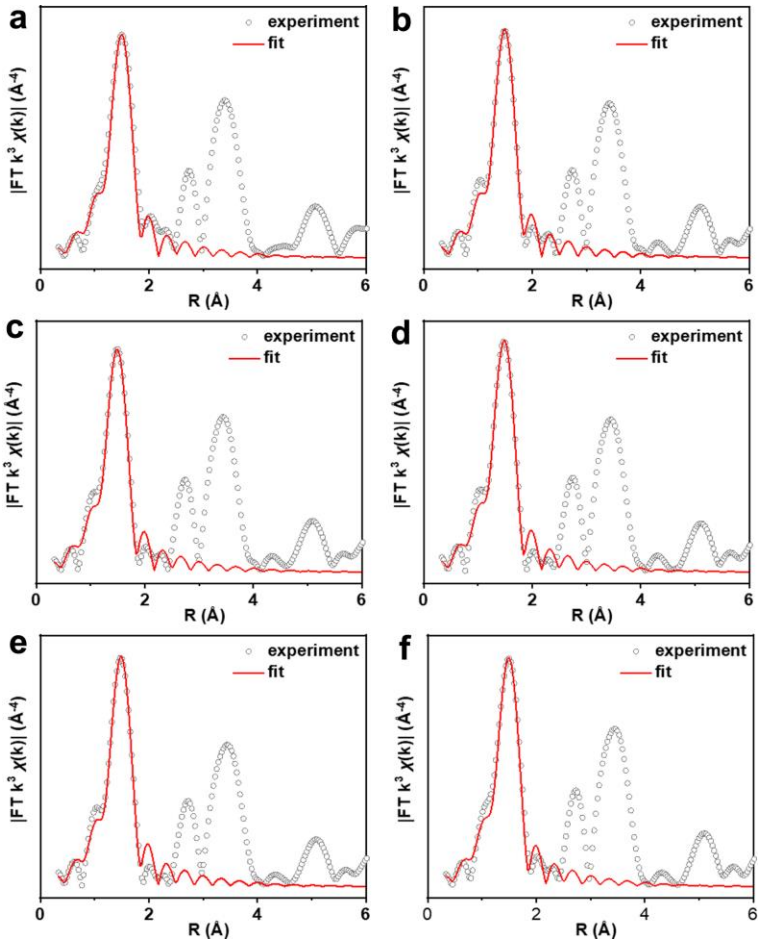

Fig. S13. XAFS fitting curve of LSCAOs. (a) x=0; (b) x=0.05; (c) x=0.10; (d) x=0.15; (e) x=0.20; (f) x=0.25. Co K-edge EXAFS (circles) and the curve-fitting (line) for LSCAOs with or without considering the case of substitutional Al atoms, shown in R-space.

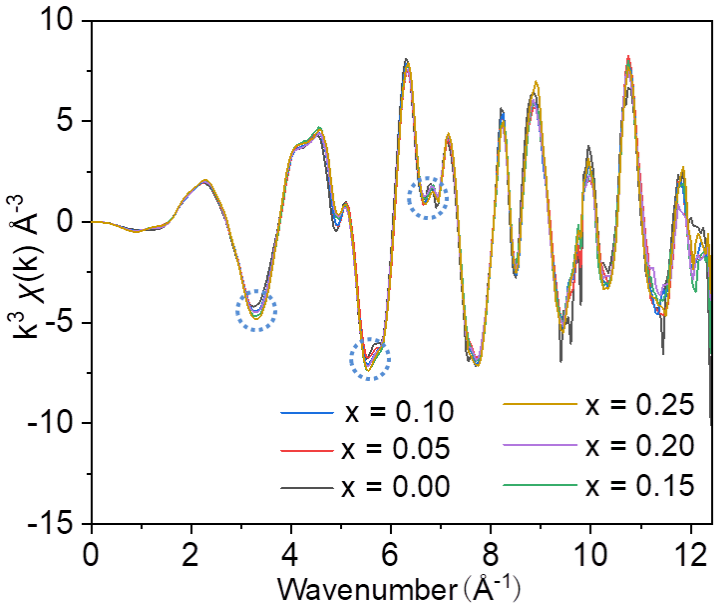

Fig. S14. Co K-edge EXAFS spectra of LSCAOs. The Co local atomic structure was investigated by extended X-ray absorption fine structure (EXAFS) analysis, certain isobestic points, such as at 5 $Å^{-1}$, are remarkable, implying a complex property with Co in different components.

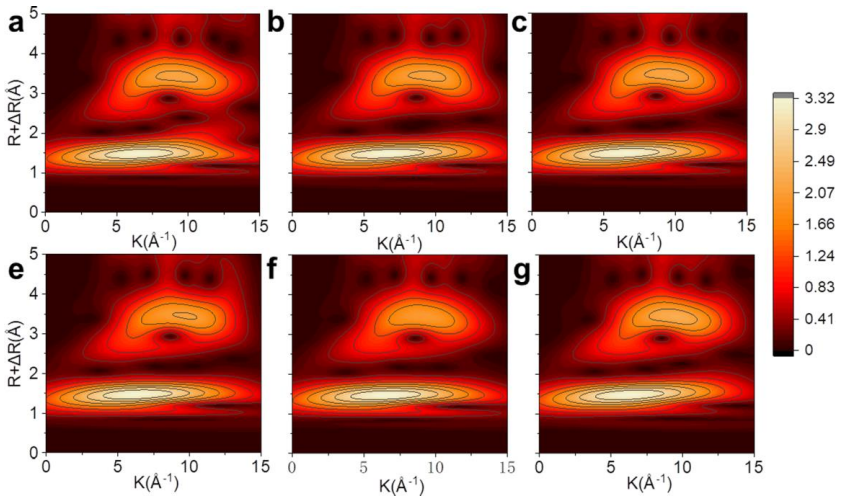

Fig. S15. Wavelet transforms for the k^3-weighted Co K-edge EXAFS signals for LSCAOs. (a) x=0; (b) x=0.05; (c) x=0.10; (d) x=0.15; (e) x=0.20; (f) x=0.25.

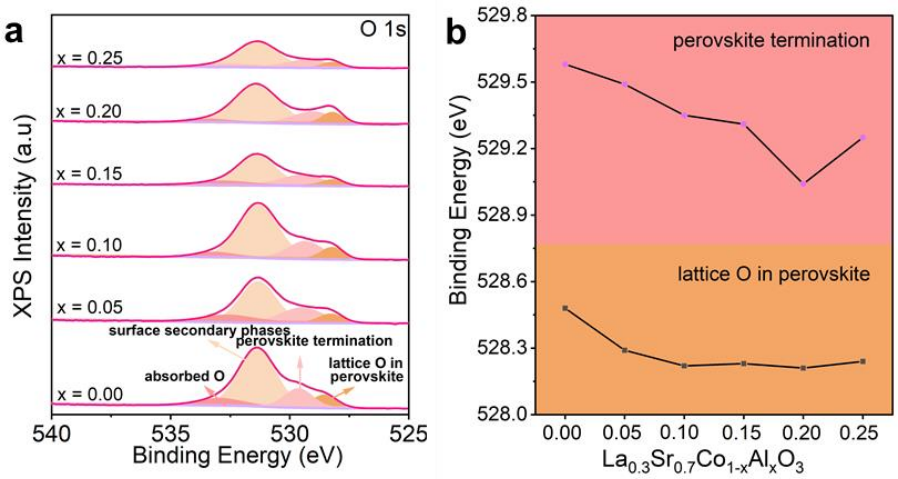

Fig. S16. The O 1*s* XPS spectra of as-prepared series of LSCAOs. (a) The O 1s XPS spectra. (b) Peak position of different oxygen species for LSCAOs with different Al substitution.

The XPS of O 1*s* can be divided into four peaks. The component located at ~ 528.4 eV belongs to surface lattice oxygen in perovskite; the one located at ~ 529.2 eV is attributed to perovskite lattice termination; the one at ~ 531.6 eV is attributed to surface secondary phases, and the one at ~ 533 eV represents the surface-adsorbed oxygen species. These samples perovskite lattice oxygen specie in LSCAOs slightly shifts to lower binding energy with the increase of Al concentration.

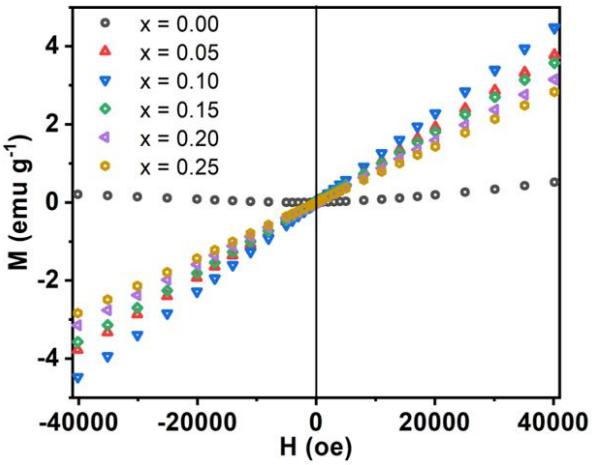

Fig. S17. Magnetic hysteresis loops of as-prepared series of LSCAOs measured at room temperature.

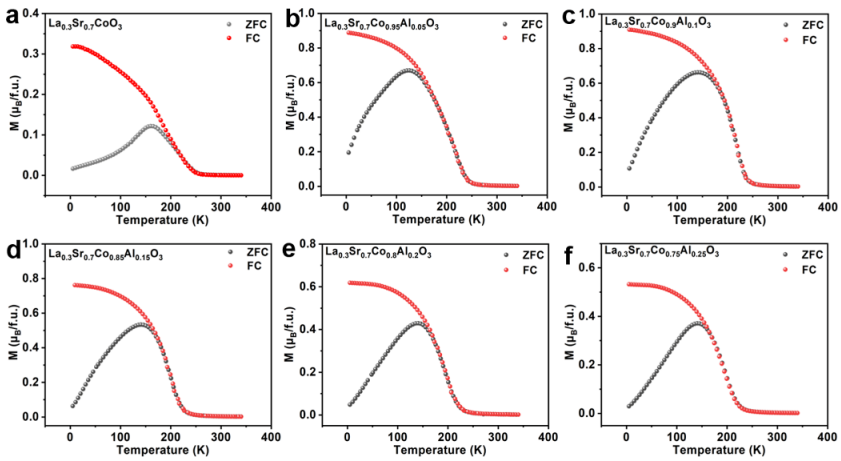

Fig. S18. The 400 Oe zero-field cooled (ZFC) and field cooled (FC) curves of LSCAOs. (a) x=0; (b) x=0.05; (c) x=0.10; (d) x=0.15; (e) x=0.20; (f) x=0.25.

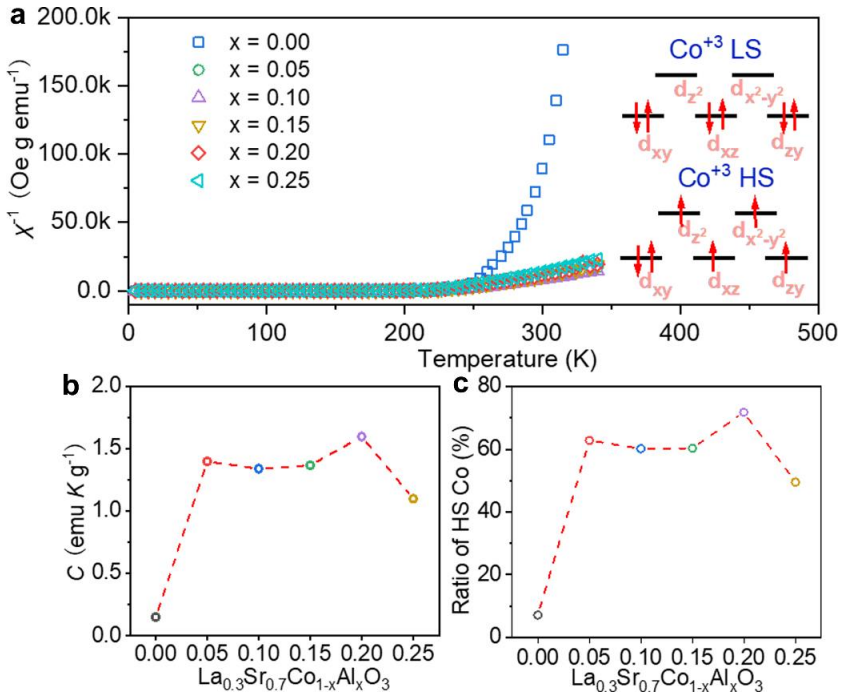

Fig. S19. Spin structure analyses of LSCAOs (x=0.00, 0.05, 0.10, 0.15, 0.20, 0.25). (a) The temperature-dependence inverse susceptibilities. The inset are the plots for Co^{3+} LS (t_{2g}^6 e_g^0, S = 0) and Co^{3+} HS (t_{2g}^4 e_g^2, S = 2) in the octahedral ligand-field. Trend in (b) curie constant and (c) the ratio of HS Co^{3+} with Al substitution.

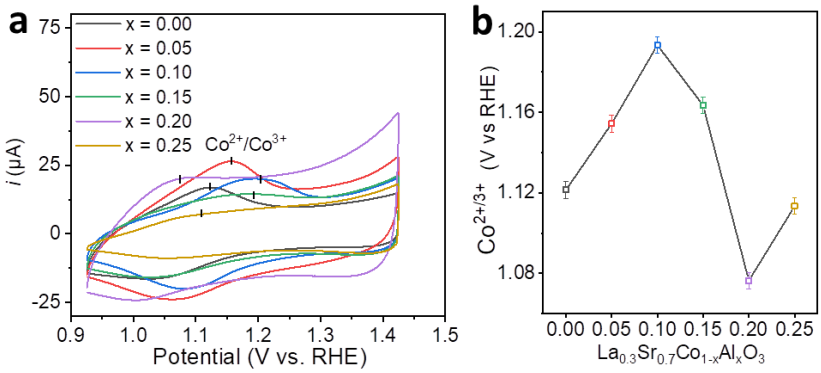

Fig. S20. CV test of LSCAOs. (a) CV curves of LSCAOs ($x \approx 0–0.25$) in O_2-saturated 1 M KOH with a scan rate of 10 mV s^{-1} between 0.95 and 1.4 V versus RHE. (b) Trend inthe oxidation peaks of the Co^{2+}/Co^{3+} redox with Al substitution. The upper imit of the potential window is capped to show the pseudocapacitive behaviour preceding to OER.

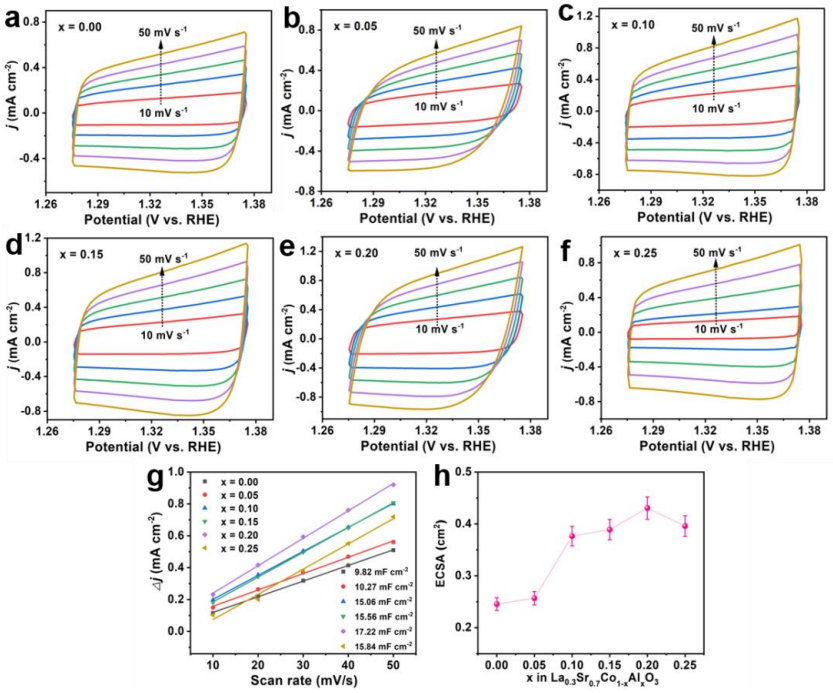

Fig. S21. DLC test of LSCAOs. (a) x=0; (b) x=0.05; (c) x=0.10; (d) x=0.15; (e) x=0.20; (f) x=0.25. (g) C_{dl} of those materials and (h) trend of ECSA with Al substitution.

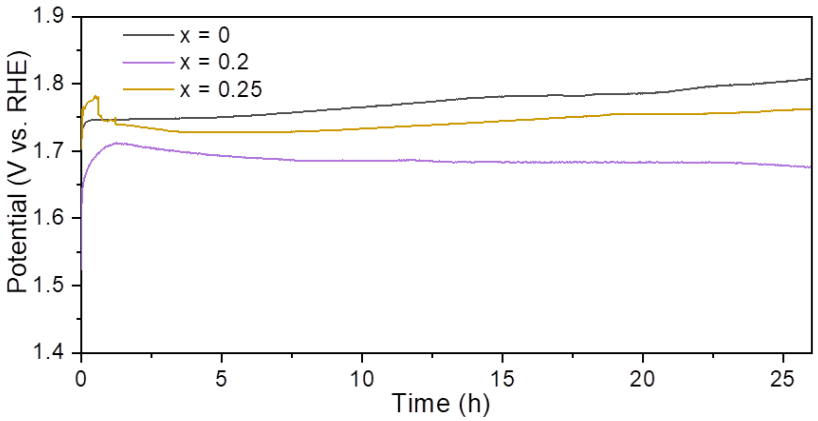

Fig. S22. Longterm stability tests of LSCAOs. Chronopotentiometry of the LSCO, LSCAO-0.2 and LSCAO-0.25 at 10 μA cm_{ox}^{-2} in 1M KOH electrolyte.

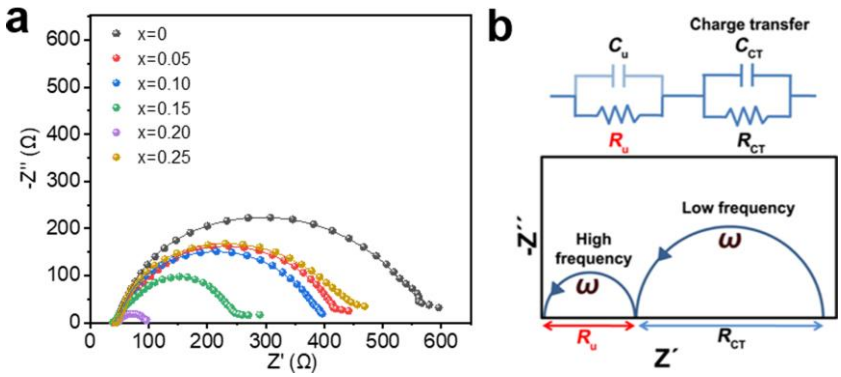

Fig. S23. EIS test of LSCAOs. (a) EIS of different LSCAOs (x ≈ 0 – 0.25) sample at a positive potential of 1.6 V versus RHE. The dotted line represents the original data, and the ball represents the fitted data. (b) The equivalent circuit model. Electrochemical impedance spectroscopy (EIS) was carried out to examine the electrical charge transfer behavior between the catalyst film and electrolyte solutions.

The complex-plane Nyquist plots acquired from the EIS and equivalent circuit for sample thin films. Moreover, the change of corresponds to the uncompensated resistance (R_U) between the working electrode and the reference electrode is not significant. In contrast, the catalyst film samples forming the heterogeneous interface have significant differences in the low-frequency second semicircle diameter representing the charge transfer resistance (R_{CT}) at the interface between the catalyst film and the electrolyte (3–5).

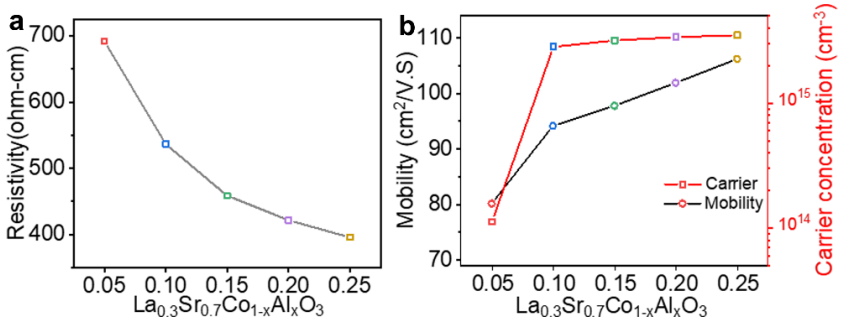

Fig. S24. The charge interaction in the LSCAOs is explored by electrical transport measurements. (a) The resistivity of LSCAOs with different Al substitution. (b) Carrier concentration and Hall mobility of the LSCAOs with Al substitution at room temperature; for more detail see Table S7.

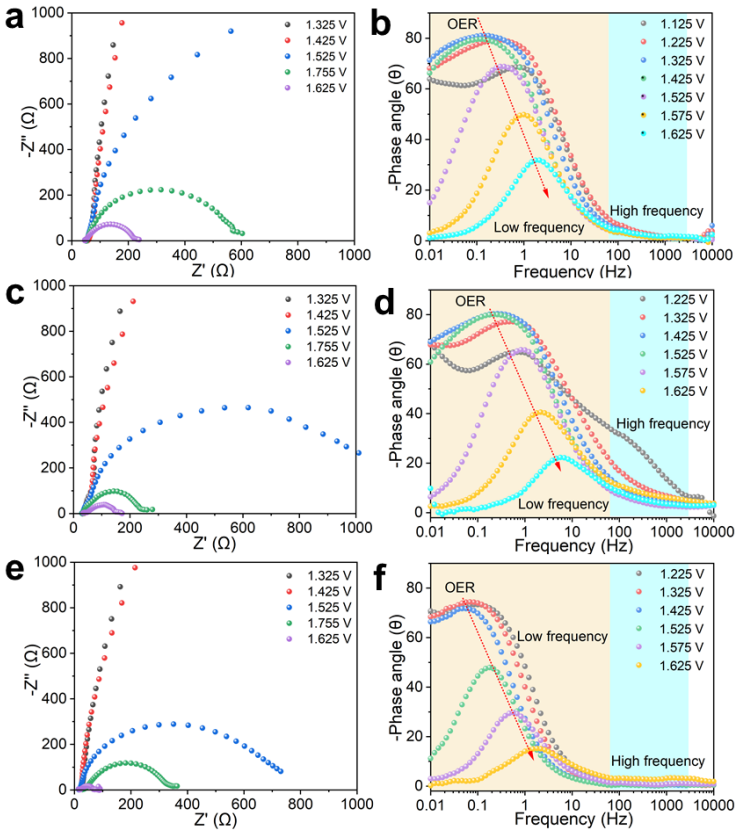

Fig. S25. *In situ* EIS test of LSCAOs. Nyquist plots and Phase angle vs log (frequency) plots of EIS data recorded at various voltages for (a, b) LSCO, (c, d) LSCAO-0.1 and (e, f) LSCAO-0.2 catalysts at different applied potentials *versus* RHE in 1 M KOH electrolyte. The peak at low-frequency region (10^0 – 10^1 Hz) should be related to the OER.

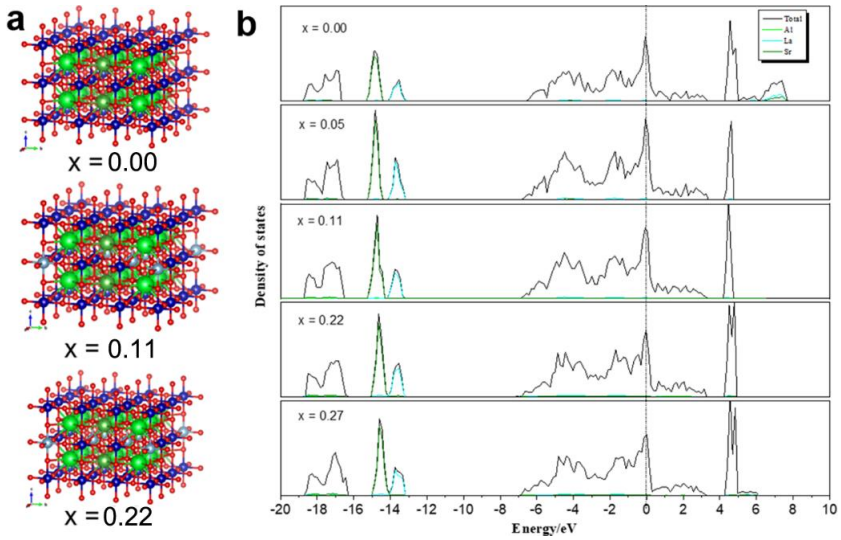

Fig. S26. (a) Computational models of LSCAOs: x = 0; 0.11; 0.22. (b) The PDOS Al, La and Sr in LSCAOs.

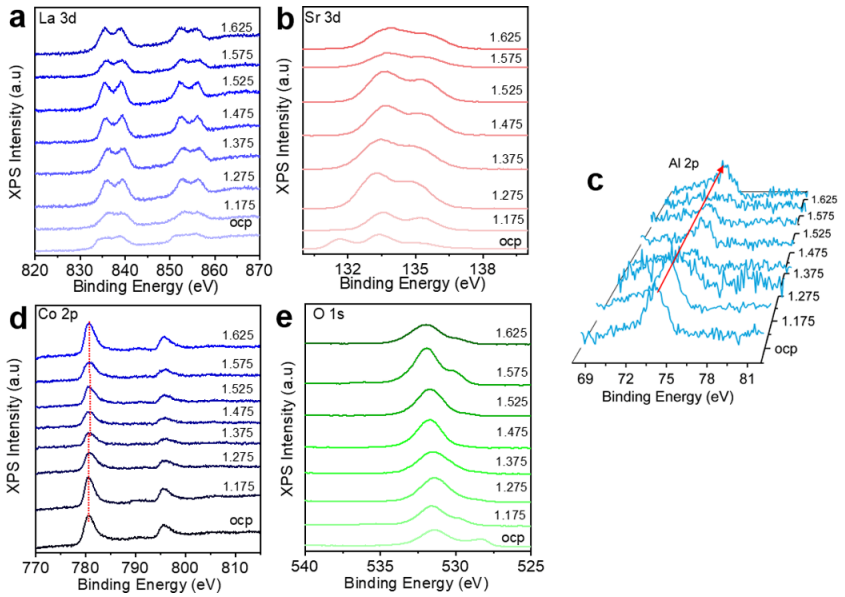

Fig. S27. Quasi *in-situ* (a) La 3*d*; (b) Sr 3*d*; (c) Al 2*p*; (d) Co 2*p*; (e) O 1s XPS spectra for LSCAO-0.2 at specific potential from 1.02 V to 1.625 V (vs. RHE).

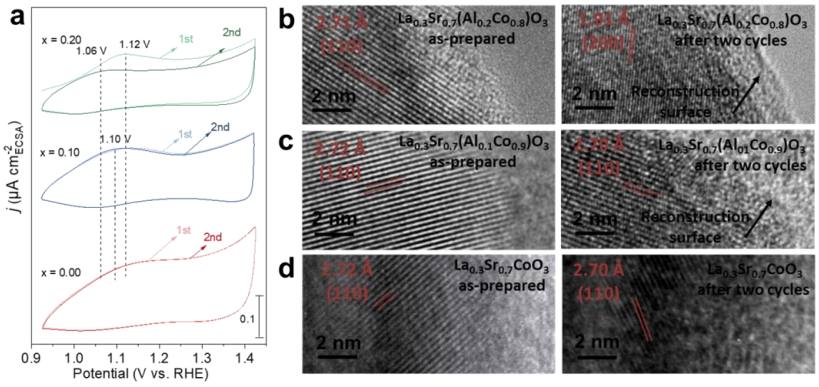

Fig. S28. *In situ* investigation of pre-OER behaviours of catalysts. (a) Pseudocapacitive behaviour in the first and second cycles of LSCO, LSCAO-0.1 and LSCAO-0.2 during CV cycling. HRTEM images, showing the surface regions for (b) as-prepared LSCO and after two cycles, (c) as-prepared LSCAO-0.1 and after two cycles and (d) as-prepared LSCAO-0.2 and after two cycles.

For LSCAO-0.2, the first cycle displays a larger pseudocapacitive charge than the second cycle, and the CV profiles exhibit negligible changes during subsequent cycles. This electrochemical behaviour suggests that the surface of the catalysts might undergo an irreversible surface reconstruction into the oxyhydroxide, evolving a stable catalytic surface for the OER. In addition, we found that the oxyhydroxide formation here displays different pseudocapacitive behaviours depending on the environments of Al species.

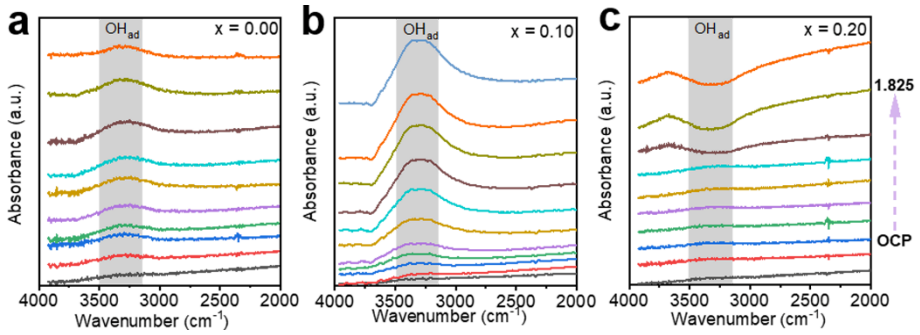

Fig. S29. *In situ* ATR-IR spectra recorded during the multi-potential steps for (a) LSCO (b) LSCAO-0.1 and (c) LSCAO-0.2. The absorption band peaked at around 3400 cm^{-1} is ascribed to the O−H stretching mode of surface-adsorbed superoxide (OH_{ad}) (6).

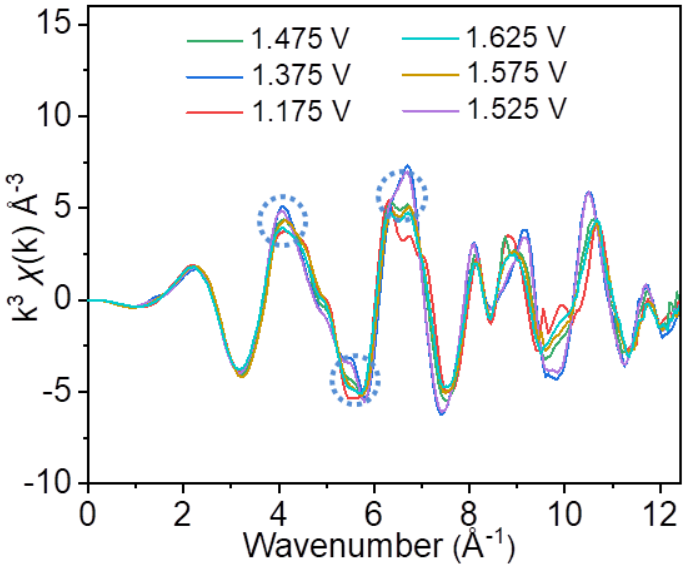

Fig. S30. Co K-edge EXAFS spectra of LSCAO-0.2 at different applied potentials *versus* RHE in 1 M KOH electrolyte.

The Co local atomic structure was investigated by extended X-ray absorption fine structure (EXAFS) analysis, certain isobestic points, such as at 5.5 $Å^{-1}$, are remarkable, implying a complex property with Co in different components.

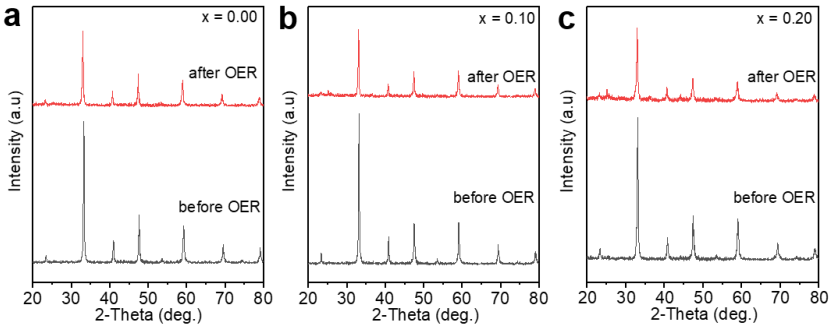

Fig. S31. XRD of before and after OER for CV-50 (a) LSCO, (b) LSCAO-0.1 and (c) LSCAO-0.2.

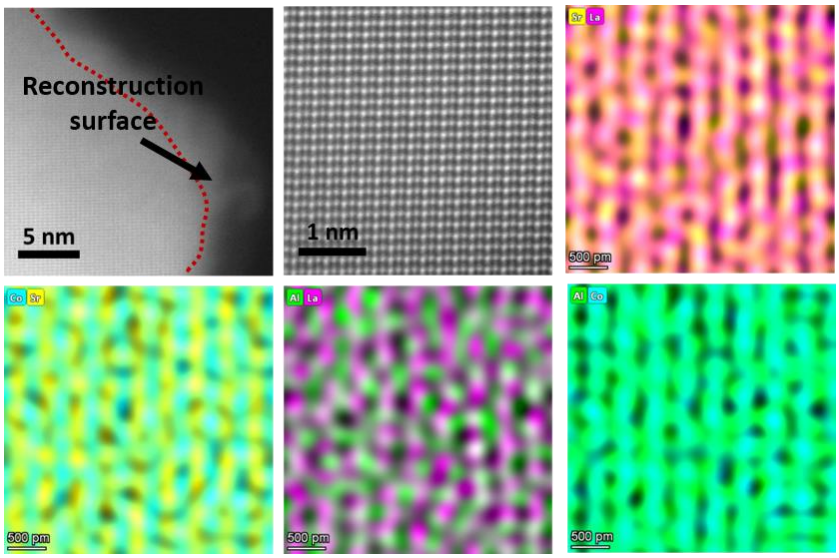

Fig. S32. Atomic-resolution HAADF-STEM image of the partially inverse for perovskite structure observed along [001] orientation and EDS atomic elemental mappings of after OER for CV-50 LSCAO-0.2.

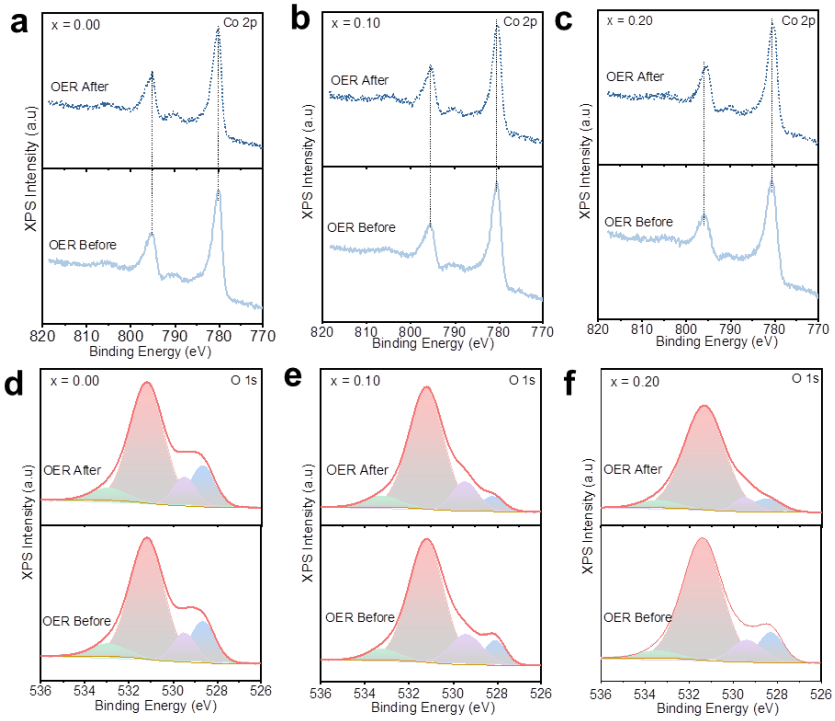

Fig. S33. XPS of before and after OER for CV-50 (a, d) LSCO, (b, e) LSCAO-0.1 and (c,f) LSCAO-0.2.

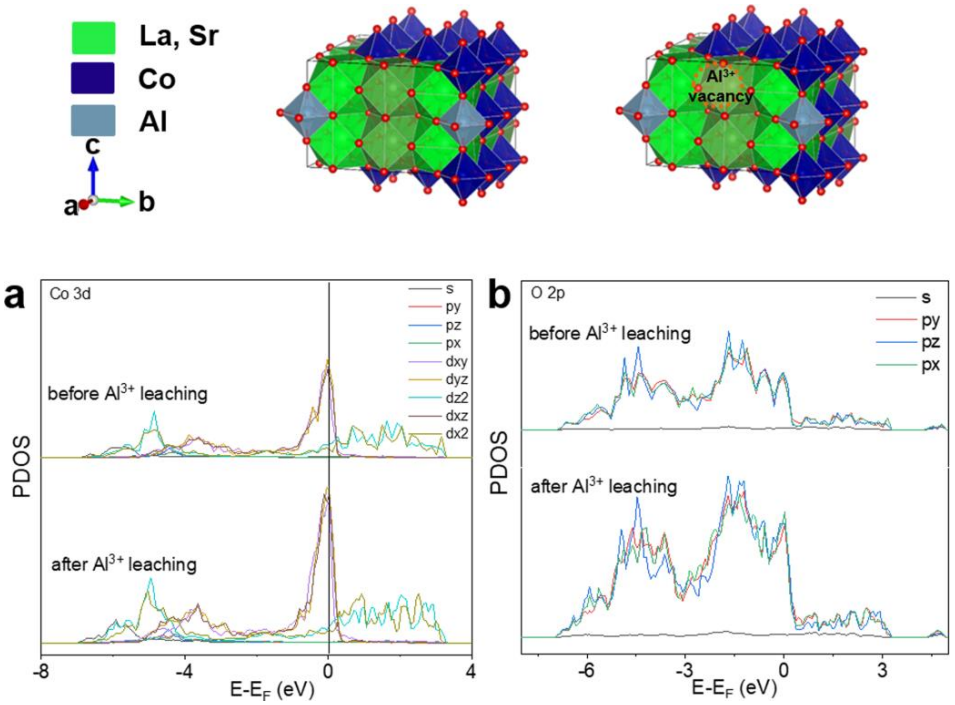

Fig. S34. PDOS of different (a) Co 3*d* and (b) O 2*p* orbitals in LSCAO-0.2 before and after Al^{3+} leaching.

Table S1. ICP-OES results for La, Sr, Co, Al and O elemental atomic percentage of $La_{0.3}Sr_{0.7}Co_{1-x}Al_xO_{3-\delta}$ catalysts.

$La_{0.3}Sr_{0.7}Co_{1-x}Al_xO_{3-\delta}$	La[mg L^{-1}]	Sr[mg L^{-1}]	Co[mg L^{-1}]	Al [mg L^{-1}]	La : Sr	Co : Al
x = 0.00	43.84	71.94	67.22		0.38	
x = 0.05	48.50	78.21	68.21	1.604	0.39	19.12
x = 0.10	49.23	78.55	64.28	3.148	0.39	9.33
x = 0.15	44.02	72.16	56.37	4.335	0.38	5.94
x = 0.20	44.28	71.26	53.46	5.723	0.39	4.26
x = 0.25	48.63	80.36	54.98	7.843	0.38	3.20

Table S2. The Co K-edge positions, nominal Co valence state and the nominal oxygen vacancy concentration (δ) in $La_{0.3}Sr_{0.7}Co_{1-x}Al_xO_{3-\delta}$.

	Co K-edge		Nominal oxygen vacancy concentration (δ)
	Edge energy (eV)	Nominal Valence state	
x = 0.00	7722.80027	2.85386	0.28205
x = 0.05	7722.81261	2.85613	0.27923
x = 0.10	7722.92926	2.87762	0.27005
x = 0.15	7723.00404	2.8914	0.2641
x = 0.20	7722.95319	2.89203	0.26479
x = 0.25	7723.04891	2.89967	0.25842

Table S3. The first-shell fitting results of Co K-edge EXAFS of $La_{0.3}Sr_{0.7}Co_{1-x}Al_xO_{3-\delta}$.

	Average co-ordination number	R (Å)	σ^2
x = 0.00	6.000	1.91195	0.00308
x = 0.05	5.96	1.90653	0.00275
x = 0.10	5.89	1.90727	0.00340
x = 0.15	5.81	1.90362	0.00344
x = 0.20	5.73	1.90348	0.00314
x = 0.25	5.69	1.90953	0.00361

Table S4. XPS fitting analysis for the O 1s in $La_{0.3}Sr_{0.7}Co_{1-x}Al_xO_{3-\delta}$.

$La_{0.3}Sr_{0.7}Co_{1-x}Al_xO_{3-\delta}$	Peak	Position (eV)	Area%	FWHM (eV)	GL (%)
x = 0.00	0	528.48	10.01	1.24	30
	1	529.58	15.84	1.34	30
	2	531.31	65.60	1.78	30
	3	532.91	8.56	2.16	30
x = 0.05	0	528.24	6.08	0.89	30
	1	529.25	19.52	1.92	30
	2	531.36	65.98	1.94	30
	3	532.72	8.42	2.66	30
x = 0.10	0	528.22	8.13	1.07	30
	1	529.35	18.67	1.66	30
	2	531.33	68.15	1.89	30
	3	533.22	5.06	1.86	30
x = 0.15	0	528.80	8.81	1.01	
	1	529.51	23.37	2.05	30
	2	531.38	61.08	1.81	30
	3	532.80	8.81	2.44	30
x = 0.20	0	528.21	9.20	0.98	30
	1	529.04	18.17	1.89	30
	2	531.41	68.86	2.10	30
	3	533.49	3.76	2.03	30
x = 0.25	0	528.24	6.08	0.89	30
	1	529.25	19.52	1.92	30
	2	531.36	65.98	1.94	30
	3	532.73	8.42	2.66	30

Table S5. Effective magnetic moment (μ_{eff}) for different spin states of Co ions in $La_{0.3}Sr_{0.7}Co_{1-x}Al_xO_{3-\delta}$ (x = 0.00, 0.05, 0.10, 0.15, 0.20, 0.25) (LS: low spin; HS: high spin).

$La_{0.3}Sr_{0.7}Co_{1-x}Al_xO_{3-\delta}$			x = 0.00	x = 0.05	x = 0.10	x = 0.15	x = 0.20	x = 0.25
Curie Constant			0.1504	1.397	1.339	1.3661	1.595	1.099
Spin state	LS	HS	7.1%HS 92.9%LS	62.8%HS 37.2%LS	60.2%HS 39.8%LS	60.3%HS 39.7%LS	71.8%HS 28.2%LS	49.5%HS 50.5%LS
μ_{eff} (μB)	0	4.9	0.779	2.373	2.324	2.348	2.536	2.105

Table S6. The Hall measurements for those of $La_{0.3}Sr_{0.7}Co_{1-x}Al_xO_{3-\delta}$ catalysts.

$La_{0.3}Sr_{0.7}Co_{1-x}Al_xO_{3-\delta}$	Temperature (K)	Resistivity (ohm-cm)	Mobility ratio ($cm^2/V.S$)	Carrier concen-tration ($1/cm^3$)	Hall mobility (cm^{-3}/C)	*f*
x = 0.00	298	1.24E-01	5.31E+00	9.52E+18	6.57E-01	1.00E+00
x = 0.05	298	6.92E+02	8.02E+01	1.13E+14	-5.55E+04	9.82E-01
x = 0.10	298	5.37E+02	9.42E+01	2.83E+15	-5.88E+02	9.91E-01
x = 0.15	298	4.59E+02	9.78E+01	3.18E+15	-3.42E+03	9.62E-01
x = 0.20	298	4.22E+02	1.02E+02	3.39E+15	-7.04E+02	9.62E-01
x = 0.25	298	3.96E+02	1.06E+02	3.50E+15	-9.62E+02	9.63E-01

Table S7. The DFT calculated energy of Co 3*d* band center and O 2*p* band center of $La_{0.3}Sr_{0.7}Co_{1-x}Al_xO_{3-\delta}$ (x=0.0, 0.05, 0.11, 0.22 and 0.27) relative to Fermi level.

$La_{0.3}Sr_{0.7}Co_{1-x}Al_xO_{3-\delta}$	Co 3*d* (eV)	O 2*p* (eV)	Co 3*d* – O 2*p* (eV)
x = 0.00	-1.756	-2.183	0.427
x = 0.05	-1.9926	-2.3998	0.4072
x = 0.11	-1.91282	-2.2087	0.29588
x = 0.22	-1.8421	-2.09218	0.25008
x = 0.27	-2.0165	-2.2777	0.2612
x = 0.22 (Al^{3+} leaching)	-1.8351	-2.280	0.4449

Table S8. The oxygen vacancy formation enthalpy of $La_{0.3}Sr_{0.7}Co_{1-x}Al_xO_{3-\delta}$.

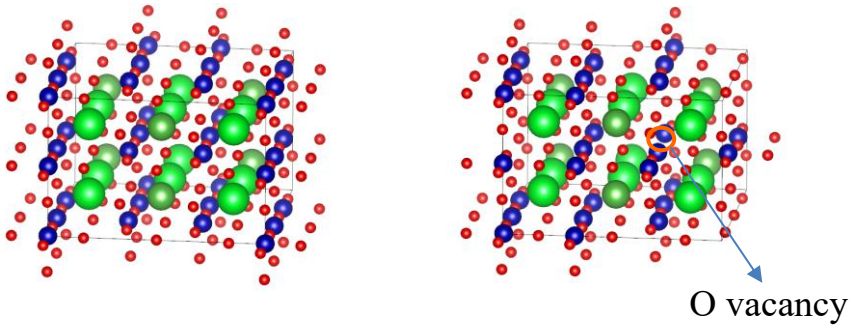

$La_{0.3}Sr_{0.7}Co_{1-x}Al_xO_{3-\delta}$	E[perfect]	E[defect]	E[O]	oxygen vacancy formation energy
x = 0.00	-534.839	-530.737	-5.0232	-0.92171425
x = 0.05	-538.34	-533.419	-5.0232	-0.10211425
x = 0.11	-541.352	-536.869	-5.0232	-0.54064425
x = 0.16	-546.956	-542.031	-5.0232	-0.09825425
x = 0.22	-548.117	-544.318	-5.0232	-1.22439425
x = 0.27	-551.932	-548.177	-5.0232	-1.26806425

References:

1. M. Duffiet, M. Blangero, P. E. Cabelguen, K. S. Song, F. Fauth, C. Delmas, D. Carlier, Probing Al Distribution in $LiCo_{0.96}Al_{0.04}O_2$ Materials Using ^{7}Li, ^{27}Al, and ^{59}Co MAS NMR Combined with Synchrotron X-ray Diffraction. *Inorg. Chem.* 59, 2890−2899 (2020).
2. H. Y. Wang, S. F. Hung, H. Y. Chen, T. S. Chan, H. M. Chen, B. Liu, In Operando Identification of Geometrical-Site-Dependent Water Oxidation Activity of Spinel Co_3O_4. *J. Am. Chem. Soc.* 138, 36–39 (2016).
3. J. Bak, H. B. Bae, S. -Y. Chung, Atomic-Scale Perturbation of Oxygen Octahedra via Surface Ion Exchange in Perovskite Nickelates Boosts Water Oxidation. *Nat. Commun. 10*, 2713 (2019).
4. P. Lacorre, J. B. Torrance, J. Pannetier, A. I. Nazzal, P. W. Wang, T. C. Huang, Synthesis, Crystal Structure, and Properties of Metallic $PrNiO_3$: Comparison with Metallic $NdNiO_3$ and Semiconducting $SmNiO_3$. *J. Solid State Chem. 91*, 225−237 (1991).
5. M. B. Stevens, L. J. Enman, A. S. Batchellor, M. R. Cosby, A. E. Vise, C. D. M. Trang, S. W. Boettcher, Measurement Techniques for the Study of Thin Film Heterogeneous Water Oxidation Electrocatalysts. *Chem. Mater. 29*, 120−140 (2017).
6. L. An, H. Zhang, J. Zhu, S. Xi, B. Huang, M. Sun, Y. Peng, P. Xi, C.-H. Yan, Balancing Activity and Stability in Spinel Cobalt Oxides through Geometrical Sites Occupation towards Efficient Electrocatalytic Oxygen Evolution *Angew. Chem. Int. Ed.* 62, 202214600 (2022).